Characterization of silica-PEG-CaCl2 composite sorbents in an open thermochemical heat storage reactor

Elise Bérut, Laurence Bois, Quentin Touloumet, Jonathan Outin, Michel Ondarts, Georgeta Postole, María José Rueda López, Aline Auroux, Nolwenn Le Pierrès

Characterization of silica-PEG-$CaCl_2$ composite sorbents in an open thermochemical heat storage reactor

Elise Bérut [a], Laurence Bois [b], Quentin Touloumet [c], Jonathan Outin [a], Michel Ondarts [a], Georgeta Postole [c], María José Rueda López [a], Aline Auroux [c], Nolwenn Le Pierrès [a,*]

[a] LOCIE Laboratory, UMR 5271, Université Savoie Mont-Blanc, CNRS, 73370 Le Bourget-du-Lac, France
[b] Université Claude Bernard Lyon 1, CNRS, LMI UMR 5615, 69622 Villeurbanne, France
[c] Université Claude Bernard Lyon 1, CNRS, IRCELYON UMR 5256, 69626 Villeurbanne, France

*Corresponding author. E-mail address: nolwenn.le-pierres@univ-smb.fr (N. Le Pierrès)

Abstract

Composite sorbents based on silica, polyethylene glycol (PEG) and containing calcium chloride were successfully synthetized using the sol-gel method. Their heat storage performance was investigated in a lab-scale open fixed-bed reactor. The silica / PEG matrix managed to stabilize hydrated calcium chloride when the salt content was equal to 32 wt% despite partial salt deliquescence. The presence of a crystallized phase $CaCl_2$ / PEG resulting from the complexation of the salt by the polymer may indeed prevent salt leakage, which was observed only when the salt content was increased to 42 wt%. Comparative experiments with a PEG-free control sample confirmed that the polymer enhances material stability. With a regeneration temperature of 130 °C, the best performing composite sorbent exhibited an average water sorption capacity of 0.37 g_{H2O} g^{-1} of dehydrated material and an energy density of 782 kJ kg^{-1} over four successive sorption cycles at 30 °C and 42% relative humidity. The dispersion and accessibility of the salt was enhanced after its first dissolution in the reactor. Compared to zeolite 13X, the sorption kinetics of the composite is much slower, resulting in a halved generated power. Still, the mass energy density of the composite is 70% higher than that of zeolite, which makes it a promising material for heat storage applications with moderate required power outputs.

Keywords: thermochemical heat storage, open sorption reactor, composite, calcium chloride, PEG, silica

1. Introduction

Energy generation from renewable sources such as wind or solar radiation supports infrastructure resilience and reduces vulnerability to climate change [1]. Renewable energies are clean, abundant and decentralized, but they are also intermittent in nature, thus requiring energy storage systems. These systems allow for meeting variable energy demands despite the inability to produce renewable energy for 24 h a day. Heat storage technologies can also be used for waste heat recovery. In the transport sector, for instance, the integration of heat storage systems could offer a reliable way of heating truck cabins when the engine is off. Such technology would replace auxiliary heating systems, which are fuel consuming and contribute to greenhouse gas emissions.

Since energy is mostly used for heating and cooling applications [2-3], thermal energy storage has been extensively investigated. It includes sensible, latent and thermochemical heat storage. The latter is particularly attractive because heat is stored as chemical potential energy, which prevents heat loss during long-term storage. Besides, thermochemical energy storage (TCES) systems are able to achieve high energy densities [4]. However, they are still in the early stage of development. TCES

systems are based on reversible sorption phenomena involving chemical and physical bonding: the phenomena for charging and discharging heat are endothermic and exothermic, respectively.

The viability of TCES systems depends on many parameters, including the energy density of the storage material. Developing high energy density materials is essential for the systems to be compact and thus suitable for a wide range of applications, especially in the residential or in the transport sector. The most promising materials in this regard are salt hydrates [5-6], but their performance under actual operating conditions is unsatisfactory, mainly because of agglomeration, melting or deliquescence leading to poor heat and mass transfer [7,8].

A classical approach to solve this issue is to add a matrix to the salt [9]. The matrix should promote water-salt sorption interactions and be able to hold the salt and its solutions within its internal pore system [5,7]. Different matrixes have been considered such as silica gel, zeolite, expanded graphite, activated carbon, metal foams, clay or vermiculite [5,10]. The amount of salt in such composite materials is often limited and the rigidity of the matrix can be an issue considering expansion of the salt during the hydration reaction.

Calcium chloride salt has a high energy density (up to 800 kWh m^{-3}) [11], but the pure salt would melt in actual operating conditions. In this work, we chose to trap this salt in a hybrid inorganic / organic matrix, consisting of silica and polymer. Calcium chloride encapsulation inside silica has often been considered for TCES applications [12-14], but the combination of silica and polymer to stabilize the salt has never been reported so far. The presence of polymer gives elasticity and flexibility to composites [15-17]. More importantly, the polymer could form chemical bonds with the salt, thus stabilizing it. Polyethylene glycol (PEG) polymer, which is composed of a linear dimethyl ether chain with terminal hydroxyl, was selected for this reason. PEG is often used in phase change material (PCM) applications. Its association with calcium chloride [18-19] or with silica [20] has been reported to prevent the leakage of the polymer. Here, the ability of a silica / PEG matrix to stabilize calcium chloride in thermochemical heat storage applications is assessed for the first time.

The material synthesis method proposed in this paper was inspired by the work of Nakanishi *et al.* [21-23]. In the 1990s, they developed a procedure for synthesizing porous silica for separation applications on the basis of silica-PEG composites produced by a sol-gel method. We were also inspired by a previous work [24] dealing with the development of porous coatings, in which we described phase separation phenomena in a system based on silica / PEG and assisted by calcium chloride. A two-fold strategy is proposed in this paper to stabilize the salt (calcium chloride) in a solid matrix. First, PEG is used to form a cross-linking network through the complexation reaction between PEG and $CaCl_2$ so as to limit the salt diffusion. Second, a sol-gel process is used to encapsulate the salt in a silica matrix thanks to the hydrolysis and condensation of a molecular silica precursor (TEOS).

This work aims at developing a stable and high energy density composite material for TCES. Its originality lies in (1) the idea of combining silica and polymer to stabilize the chosen salt hydrate, (2) the characterization of silica-PEG-salt composites in a lab-scale heat storage reactor and (3) the association of macro and micro scale analyses to understand the performance evolution. Two composite samples with different salt contents (32 and 42 wt% $CaCl_2$) were synthetized and compared. Their storage performance (e.g. water sorption capacity, energy density, generated power) is characterized over several cycles in a lab-scale open reactor in the conditions of a solar heat storage system for space heating in buildings. The results are compared to those obtained using PEG-free and salt-free control samples, as well as zeolite 13X and other $CaCl_2$-based composites from the literature. In addition, the textural and structural properties of the composites are investigated before and after reactor cycling in order to understand the mechanism of sorption and evaluate material stability. The water vapor sorption isotherms are also determined. Finally, the heat and water storage properties obtained inside the reactor are compared to those obtained at a smaller scale using thermogravimetry (TG) coupled with differential scanning calorimetry (DSC).

2. Materials and methods

2.1 Materials synthesis

The materials are based on a mixture of sol-gel silica, PEG filled with different amounts of a calcium chloride hydrate. The following chemicals were used: tetraethoxysilane ($Si(OEt)_4$) (Aldrich 98%), polyethylene glycol 600 (Merck), calcium chloride dihydrate $CaCl_2 \cdot 2H_2O$ (Aldrich 99%), HCl (37 wt%). The HCl solution was diluted to 3.7 wt%. The synthesis procedure is illustrated in Fig. 1. First, PEG-600 (1 g) and $CaCl_2 \cdot 2H_2O$ (1.6 g in sample 1 and 2.4 g in sample 2) were dissolved in the water solution of HCl 3.7 wt% (7 g). Then, $Si(OEt)_4$ (4 g) was added to the solution under stirring for two hours at room temperature. Acidic aqueous solution is used to induce the hydrolysis and condensation of $Si(OEt)_4$ and to form a silica phase. The PEG polymer is used to react with calcium chloride in a complexation reaction, avoiding a phase separation between calcium salt and silica after the silica gelation. The two liquid phases, i.e. $Si(OE)_4$ and the aqueous phase containing the PEG and calcium salt, are not miscible but become so after stirring for 15 min because of the hydrolysis reaction of $Si(OEt)_4$. The obtained sol was then placed in a closed container at 50 °C for 24 h, forming a gel within a few hours. Next, a slow evaporation was performed at 60 °C for 24 h and then at 100 °C for 24 h in a sand bath. The dried gel, consisting of a silica matrix containing both PEG and calcium chloride, is monolithic (Fig. 1) and crushed into pieces of a few millimeters. The theoretical composition of samples 1 and 2 is reported in Table 1. Considering the cost of each compound and the amounts required for synthesis, the cost of the composite samples is close to 200 € kg^{-1}.

As blank controls, PEG / SiO_2, $CaCl_2$ / PEG and $CaCl_2$ / SiO_2 samples were also prepared using the composition of sample 1 and removing either $CaCl_2 \cdot 2H_2O$, $Si(OEt)_4$ or PEG. They are subsequently named salt-free, silica-free and PEG-free control samples, respectively. To synthesize the salt-free (resp. PEG-free) sample, 1 g of PEG-600 (resp. 1.6 g of $CaCl_2 \cdot 2H_2O$) were dissolved in the water solution of HCl 3.7 wt% (7 g). Then, $Si(OEt)_4$ (4 g) was added to the solution. To synthesize the silica-free sample, $CaCl_2 \cdot 2H_2O$ (1.6 g) and PEG (1 g) were dissolved in the water solution of HCl (7 g). The silica-free sample is in the form of a glue. The salt-free sample looks similar to samples 1 and 2, while the PEG-free sample has the form of small pieces of gel.

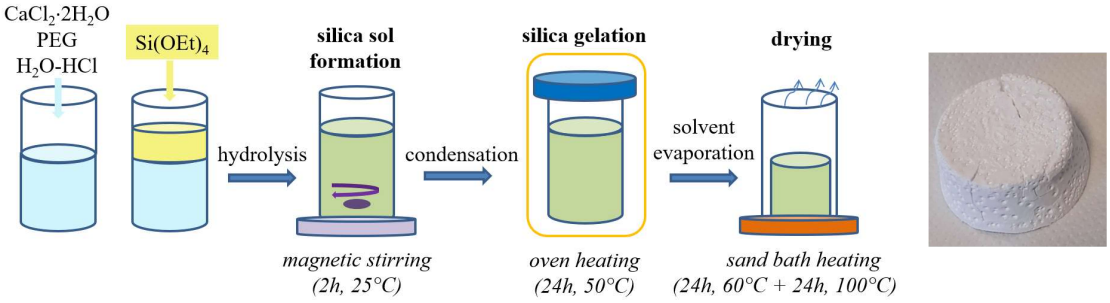

Fig. 1. Schematic illustration of the synthesis procedure (left) and resulting monolithic sample 1 (right)

Table 1. Theoretical weight composition of the synthetized samples

	anhydrous $CaCl_2$ content (wt%)	SiO_2 content (wt%)	PEG content (wt%)
Sample 1	36	34	30
Sample 2	46	29	25
Salt-free	0	54	46
Silica-free	54	0	46
PEG-free	51	49	0

2.2 Materials characterization

Elemental analysis was performed on the samples using inductively coupled plasma optical emission spectroscopy (ICP-OES) with an ACTIVA spectrometer from Horiba Jobin Yvon. The accuracy of the ICP-OES device is ± 2%. In order to dissolve them completely, the samples were treated with a mixture of inorganic acids (H_2SO_4 and HNO_3) at 300 °C.

X-ray diffraction (XRD) measurements were carried out on a PANalytical X'pert Pro diffractometer scanning from 4° to 80° (2θ) using a Cu K_α radiation source at λ = 1.54 Å. Scanning electron microscopy (SEM) images and elemental mapping with energy dispersive X-ray spectrometry (EDS) of the composite were captured by the Zeiss Merlin Compact operating at 10 kV. Infra-red spectra of the solids were recorded on Safas Monaco IR700 spectrometer.

In order to further characterize the studied composites, water vapor sorption isotherms were determined using a Micromeritics 3 Flex apparatus. Experiments were performed using 70 mg to 100 mg of solid, which was pretreated under vacuum at 150 °C for three hours. To obtain the sorption isotherm, the temperature was set to 20 °C and the relative humidity varied from 0% to 98%.

2.3 Measurement of heat and water storage properties

The heat of hydration / dehydration and the corresponding amount of water uptake / loss in composite sorbents were recorded using a thermogravimetric (TG) analyzer coupled to a differential scanning calorimeter (DSC) (Setaram SENSYS EVO TG-DSC) and to a humidity generator (Setaram WETSYS). Each experiment was conducted using about 8 mg of material placed in an open quartz cell. Three steps were performed under atmospheric pressure with an air gas flow rate set to 20 mL min^{-1}. (1) The sample was dehydrated under dry air flow at 130 °C for 3 h 35 (after a temperature rise from 25 °C at the speed of 4 °C min^{-1}). (2) After cooling to room temperature under the same gas atmosphere, hydration is carried out during 48 h under humid air flow at 25 °C and 42% RH. (3) The first step (dehydration) is repeated.

Prior to each measurement, a blank experiment was performed under the same conditions with an empty cell. The enthalpy of desorption (in kJ kg^{-1} of dehydrated material) is determined by linear integration of the heat flow signal recorded during the second dehydration (third step), after subtracting the heat flow measured during the blank experiment. The error on the evaluation of the enthalpy is around ± 20 kJ kg^{-1}. The water sorption capacity (SC) of the sample is also evaluated from the weight evolution during the second dehydration:

$$SC = \frac{W_{hs} - W_{ds}}{W_{ds}} \quad (1)$$

where W_{hs} is the weight of the wet sample (as measured after hydration) and W_{ds} is the weight of the dry sample (as measured after the second dehydration). The sorption equilibrium was considered to be reached at the end of each step since the weight change was smaller than 0.5% between consecutive 10 minutes intervals.

2.4 Lab-scale reactor cycling experiments

A test bench [25] was designed in order to characterize the storage performance of each sample in the conditions of a solar heat storage system for space heating in buildings.

2.4.1 Description of the test bench

The open-cycle sorption storage system is presented in Fig. 2. It consists in a fixed bed reactor, a direct contact bubbling humidifier and a heating apparatus. The reactor is made of stainless steel and has a 46 mm inner diameter. It is insulated using alkaline earth silicate (AES) wool and polystyrene: both layers are around 30 mm thick. The humidifier is a water tank also made of stainless steel. It

includes a smooth tube heat exchanger enabling the control of the humidification temperature by means of a thermostatic bath (Lauda Proline RP845). The heating apparatus is composed of a gas flow circulation heater (Vulcanic 10706 custom-made, power 200 W) and a glass fiber heating tape (Cole-Parmer HT-200-6, power 300 W). The latter is wrapped around the pipes to compensate for the heat loss if needed. Each heater is associated with a temperature controller (Vulcanic 30656 and Electrothermal MC810B, respectively). The air flow rate is regulated by a mass flow controller (Brooks 5851S with 0151 flow control computer), which was calibrated over the range 2 NL min^{-1} to 30 NL min^{-1}. The uncertainty in the inlet flow rate was estimated to be 0.2 NL min^{-1} when the flow rate is below 20 NL min^{-1} and 0.3 NL min^{-1} above. The relative humidity (RH) of the inlet air is below 5% at 25 °C.

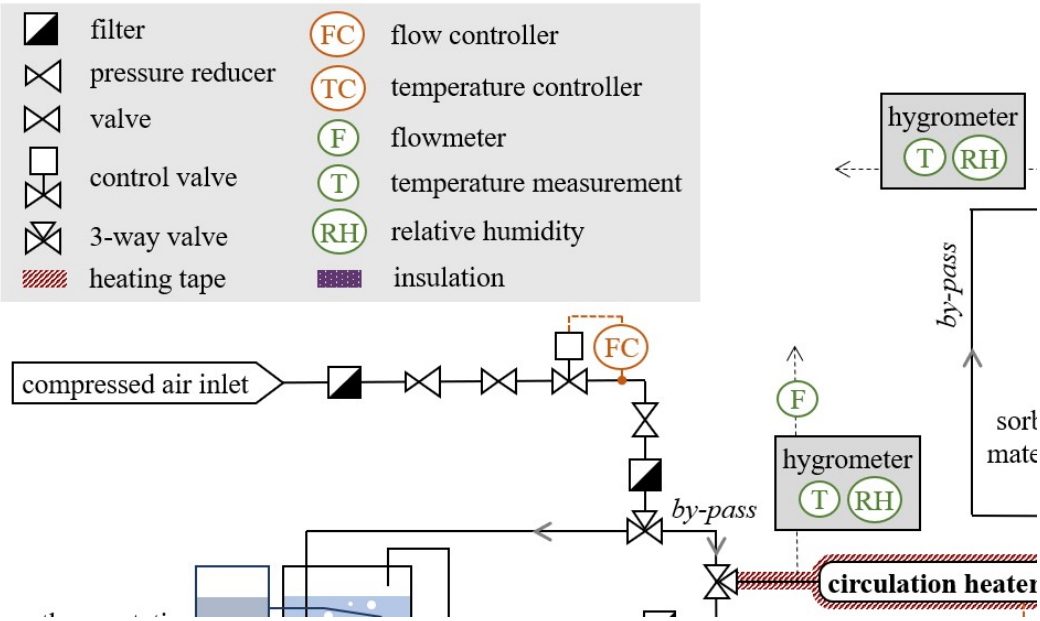

Fig. 2. Schematic of the experimental heat storage setup

The air temperature and relative humidity at the inlet and outlet of the reactor are monitored using chilled mirror hygrometers (GE Sensing Optisonde D2). The air flow rate extracted by each hygrometer is of about 1.0 ± 0.3 NL min^{-1}. The accurate determination of the flow rate going through the reactor requires the subtraction of the flow rate extracted ahead of the reactor, as well as leak tests. Such tests were conducted (with closed hygrometers) prior to the sorption experimental campaign. When varying the inlet flow rate from 4 NL min^{-1} to 30 NL min^{-1}, the leakage rate was shown to be virtually unchanged: it was estimated at 6.5% of the inlet flow rate when including the humidifier and at 5% when by-passing it.

K-type thermocouples are placed inside the reactor. Their precise location is shown in Fig. 3. They are numbered from T_1 (bottom, reactor inlet) to T_5 (top, reactor outlet). Before testing, all thermocouples were calibrated over a 5 °C to 85 °C temperature range. The resulting uncertainty in temperature measurements is ± 0.5 K. During experiments, only one thermocouple (T_2) is located inside the sorbent bed because of the limited amount of synthetized sorbent materials. Data from the thermocouples, the hygrometers and the flow controller is recorded every ten seconds using a data acquisition unit (Agilent 34972A) driven by a LabVIEW interface.

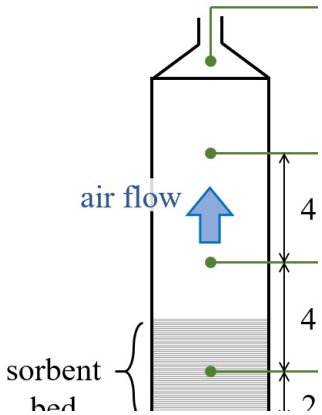

Fig. 3. Location of the thermocouples along the reactor

2.4.2 Testing procedure

Nominal experiments were conducted using 56.2 ± 4.0 g of dehydrated sample and an inlet flow rate of 9.8 ± 0.2 NL min^{-1}. When considering the air flow extracted by the first hygrometer and the leakage rate, the dry air flow rate going through the reactor is between 8.1 NL min^{-1} and 8.4 NL min^{-1}. This flow rate leads to a bulk velocity of about 0.1 m s^{-1} through the sorbent bed, which falls within the usual range for fixed bed sorption processes [5]. The pressure drop in the bed amounts to a few tens of Pascal.

During the desorption (or charging) phase, which is four hours long, the humidifier is by-passed and dry air at 130 °C is blown into the reactor to dehydrate the material. The desorption temperature was set according to the outlet temperatures easily achievable by solar air collectors [26]. Next, heating is switched off for the system to cool down. During the sorption (or discharging) phase, the air flow is first saturated with water at a given temperature by going through the bubbling humidifier, and then heated in order to reach the desired conditions at the entrance of the reactor. In this work, sorption is performed with an air flow at 30 °C (temperature T_1) and 42% RH. This temperature is higher than that usually found in residential buildings, so the storage performance will be slightly underestimated. This temperature was chosen because it can be maintained without air conditioning. Following sorption, a new desorption step is carried out to regenerate the sample and so on. Four successive desorption / sorption cycles are completed.

2.4.3 Heat and mass transfer analysis

The amount of water sorbed during each cycle is evaluated through a mass balance on the water vapor contained in the air flow. The mass balance is integrated over the duration of the sorption phase, yielding the following relation:

$$m_w = \int \dot{m}_w \, dt = \int \dot{m}_{da}(x_{in} - x_{out})dt \approx \dot{m}_{da} \sum (x_{in} - x_{out})\Delta t \quad (2)$$

where $\dot{m}_w$ is the instantaneous mass flow rate of water sorbed by the material, $\dot{m}_{da}$ is the constant dry air flow rate going through the reactor and Δt is the time interval between two measurement readings (ten seconds).

Similarly, the sensible heat given to the air flow during the sorption phase is calculated as:

$$Q_{air} = \int \dot{Q}_{air} \, dt = \int \dot{m}_{da} \, c_{p,ha}(T_4 - T_1)dt \approx \dot{m}_{da} \sum c_{p,ha}(T_4 - T_1)\Delta t \quad (3)$$

The heat capacity $c_{p,ha}$ of the *outlet* humid air is used in order to assess as closely as possible the potential for heat recovery by means of a heat exchanger placed after the reactor. Besides, temperature T_4 is considered instead of T_5 to minimize the impact of the reactor thermal loss in the calculation.

As mentioned in section 2.4.1, the air flow extracted by the first hygrometer $\dot{m}_{hygro}$ and the leakage rate $\dot{m}_{leak}$ must be considered when evaluating the dry air flow rate going through the reactor:

$$\dot{m}_{da} = \dot{m}_{tot} - \dot{m}_{hygro} - \dot{m}_{leak} \quad (4)$$

$$\text{with } \begin{cases} \dot{m}_{hygro} = \rho_{da}(P_{amb}, T_{amb})\, \dot{V}_{hygro} & (5) \\ \dot{m}_{leak} = k\, \dot{m}_{tot} & (6) \end{cases}$$

$\dot{m}_{tot}$ is the total dry air flow rate supplied at the inlet of the test bench and $\dot{V}_{hyg}$ is the volumetric flow rate measured at the outlet of the hygrometer. Since the influence of humidity on $\dot{m}_{hygro}$ is negligible in the present study, it is calculated in eq. (5) using the density of dry air seen as an ideal gas in ambient conditions. Finally, the leak coefficient k of eq. (6) was estimated to be 0.065 ± 0.043 during the sorption phase and 0.050 ± 0.030 during desorption (by-passed humidifier).

The uncertainty in each studied parameter is evaluated using the law of propagation of uncertainty, as recommended by the Joint Committee for Guides in Metrology (JCGM) [27]. It includes the precision of the measuring instruments, the reproducibility of measurements and the uncertainty due to calibrations and to property calculations. The required properties of humid air (relative and specific humidity, specific heat capacity, water vapor partial pressure) are computed using the CoolProp library [28] from the dry bulb and dew point temperatures provided by each hygrometer.

The enthalpy of sorption ΔH_s of the tested samples can be estimated from the reactor experiments and compared to that measured by thermogravimetric analysis (TGA) at the microgram scale under similar conditions. The enthalpy of sorption can be expressed (in J mol^{-1} of water) as:

$$\Delta H_s = (Q_{air} + Q_{loss})\overline{M}_w / m_w \quad (7)$$

The energy stored in the reactor wall and in the sorbent bed during the sorption phase was neglected. Indeed, according to the specific heat capacity of each element, it was estimated to be smaller than 5% of the heat given to the air flow. Conversely, the heat loss from the reactor must be considered. It can be evaluated using the following relation:

$$Q_{loss} = U \int (\bar{T} - T_{amb})dt \approx U \sum (\bar{T} - T_{amb})\Delta t \quad (8)$$

The overall heat transfer coefficient U between the ambient and the isolated reactor was determined experimentally in steady state using an inert material. It is about 0.0285 W K^{-1}. $\bar{T}$ is calculated at each time step as the average temperature of T_1, T_2, T_3 and T_4.

3. Results and discussion

This section is first devoted to the characterization of the textural and structural properties of the samples (section 3.1), both before and after reactor cycling experiments. The water vapor sorption isotherms were also determined before and after cycling. The results are presented and discussed in section 3.2. Next, section 3.3 focuses on the analysis of TG-DSC results. The heat and water storage properties provided by TG-DSC measurements (using samples of a few milligrams) are compared to those obtained inside the reactor (containing 56 g of sorbent material). Finally, the performance of the synthetized composite materials through cycling experiments on a lab-scale reactor is analyzed in section 3.4. The obtained storage performances are also compared to those of zeolite 13X and other $CaCl_2$-based composite sorbents from the literature.

3.1 Evolution of textural and structural properties

ICP-OES elemental analysis provided the salt content of samples 1 and 2 (Table 2). Before cycling, the values are somewhat lower than those estimated from the synthesis protocol (Table 1), but the salt content of sample 2 is still 10% higher than that of sample 1. After cycling, the salt content of sample 1 is unchanged. In contrast, the salt content of sample 2 decreases significantly because of salt leakage during the cycling experiments. Some salt was indeed discovered outside the reactor when the

system was opened after completing the experimental campaign. The final salt content of sample 2 is close to that of sample 1.

Table 2. Measured salt content of studied samples

	$CaCl_2$ content (wt%)	deviation from theoretical content
Sample 1	32 ± 2	-11%
Sample 1 after cycling	31 ± 2	-14%
Sample 2	42 ± 2	-9%
Sample 2 after cycling	33 ± 2	-28%

Fig. 4 shows the diffractogram of each studied composite. The X-ray diffraction patterns of samples 1 and 2 display numerous well-resolved peaks characteristic of a crystallized compound. This crystallized phase results from the complexation of the salt by the polymer and coincides with that obtained in the $CaCl_2$ / PEG control and with that previously observed [29-30]. It differs from a simple calcium chloride phase as can be seen from the comparison with the $CaCl_2$ / SiO_2 diagram, consisting in a mixture of $CaCl_2 \cdot 2H_2O$ (JCPDS 01-01-70-0385) and $CaCl_2 \cdot 4H_2O$ (JCPDS 01-072-1015). FTIR analysis (Fig. 5) confirms the complexation of the salt by the polymer, as seen in the red shift of the C-O vibrations from 1096 cm^{-1} in the PEG sample to 1048 cm^{-1} in samples 1, 2 and in the control sample $CaCl_2$ / PEG [30]. According to Fig. 4, the diffraction patterns of samples 1 and 2 before and after cycling are identical, so their crystallographic structure is unchanged.

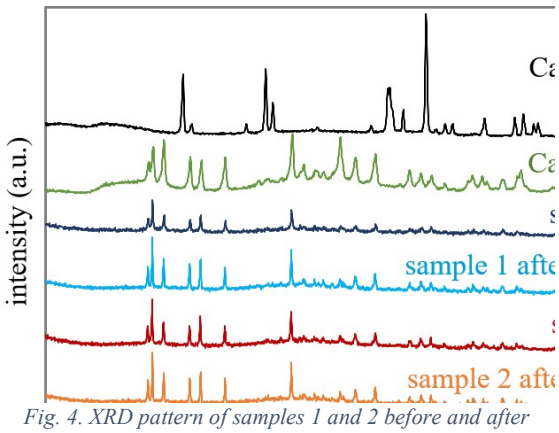

Fig. 4. XRD pattern of samples 1 and 2 before and after reactor cycling experiments

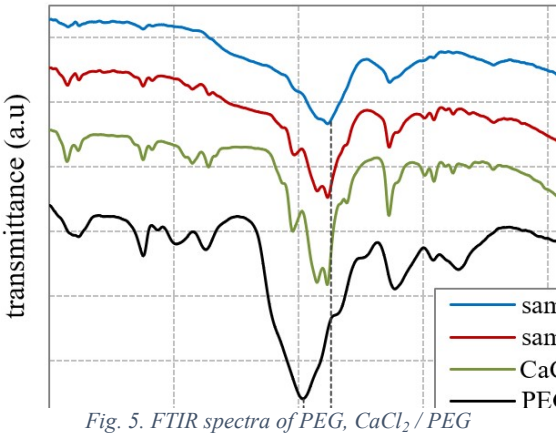

Fig. 5. FTIR spectra of PEG, $CaCl_2$ / PEG and samples 1 and 2 before cycling

The texture of sample 1 was observed by SEM (Fig. 6). Before cycling, EDX analysis shows homogeneity in the distribution of constituents since the elemental maps of carbon, calcium, chlorine and silicon are equivalent. After cycling, sample 1 has only partially retained its homogeneity. Silica is indeed observed in isolated micrometric areas. This decrease in homogeneity can be explained by the mobility of the calcium chloride rich phase during its hydration. The texture of sample 1 differs greatly from that of the $CaCl_2$ / SiO_2 control sample (Fig. 7), in which a clear heterogeneity is observed between hydrated $CaCl_2$ crystals and silica clusters of several tens of microns. The SEM images of Fig. 8 have a lower magnification: they show the morphology of the samples more distinctly. SEM images of the silica-free ($CaCl_2$ / PEG) and salt-free (PEG / SiO_2) control samples were also appended to this paper as supplementary material. According to nitrogen adsorption isotherm experiments, the samples do not contain any micropores or mesopores (< 50 nm).

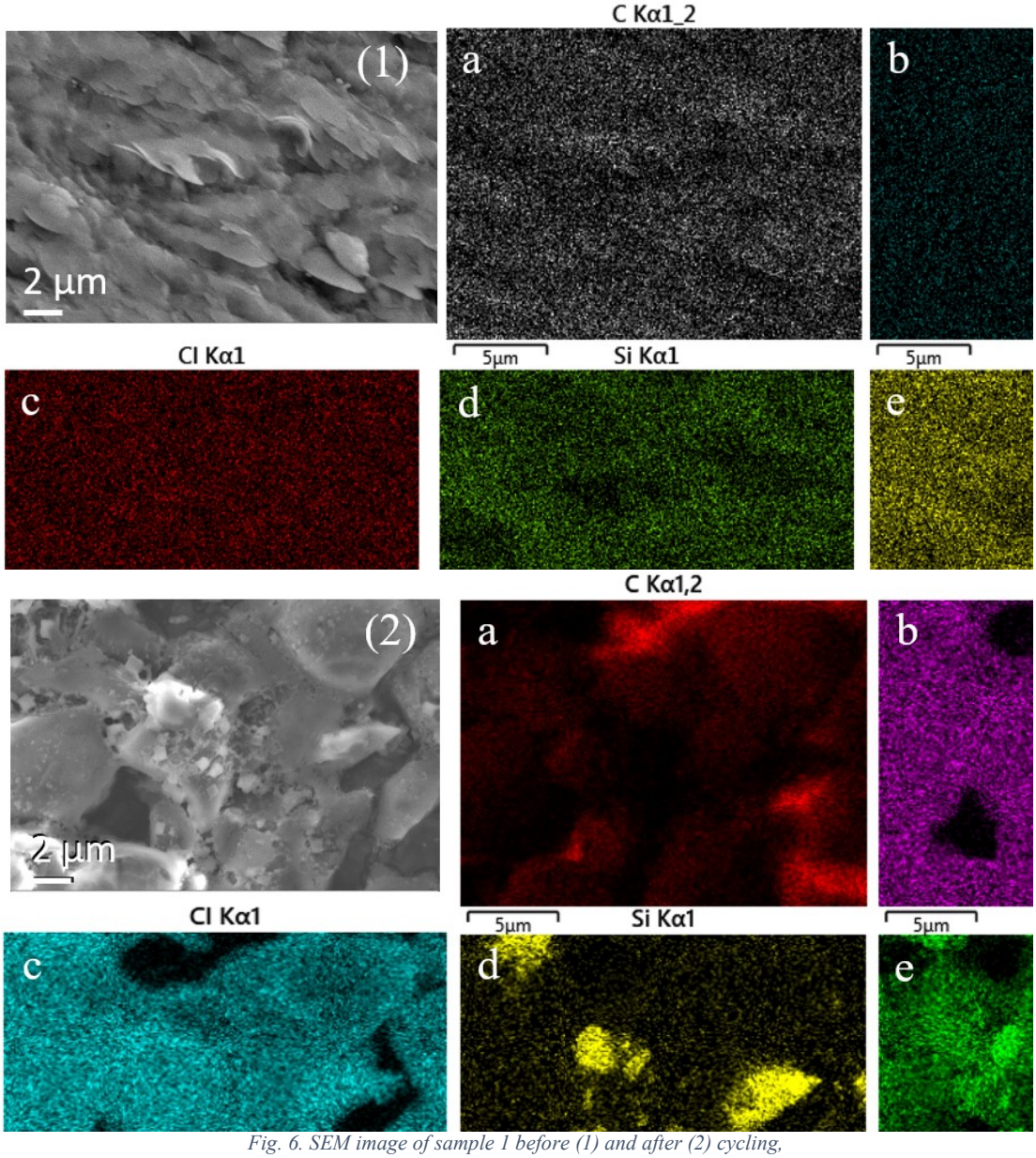

Fig. 6. SEM image of sample 1 before (1) and after (2) cycling,
and associated elemental mapping of carbon (a), calcium (b), chlorine (c), silicon (d) and oxygen (e) by EDS

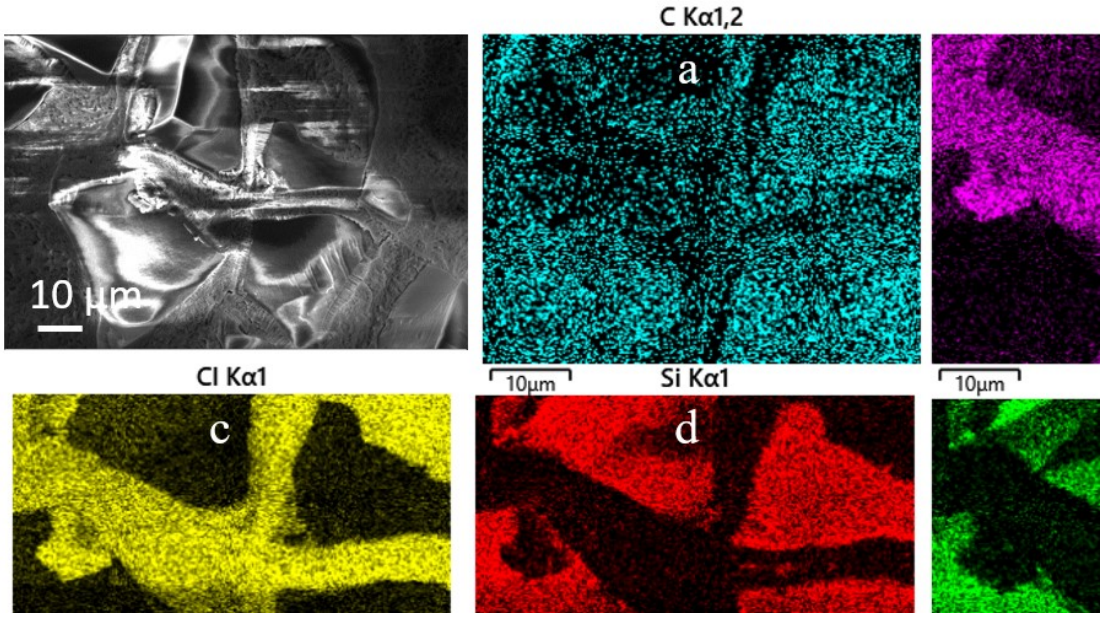

Fig. 7. SEM image of the PEG-free control sample ($CaCl_2$ / SiO_2) before cycling, and associated elemental mapping of carbon (a), calcium (b), chlorine (c), silicon (d) and oxygen (e) by EDS

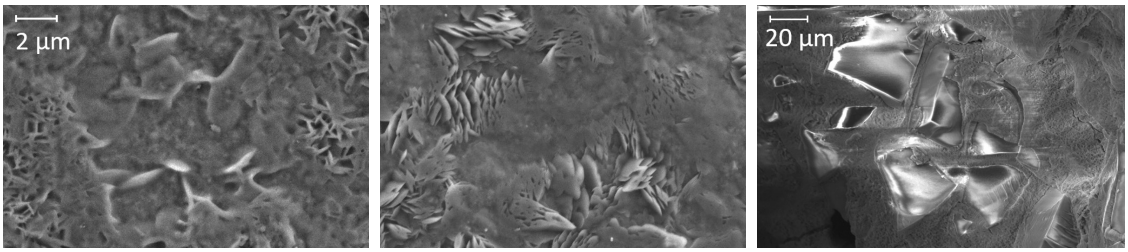

Fig. 8. SEM images of (left) sample 1, (center) sample 2 and (right) the PEG-free control sample

Finally, the macroscopic texture of samples 1 and 2 after sorption is really different from their initial dehydrated aspect (Fig. 9). Initially dry, hard and brittle, the materials become soggy, sticky and visibly saturated with water. Still, the handling of the samples is relatively easy, both in their dehydrated and hydrated form. They can be easily poured from one container to another. During hydration, some aggregates form as the volume of the grains increases. This reduces the intergranular porosity which, in turn, potentially increases the pressure drop. However, the intergranular porosity may be controlled by adjusting the initial size of the grains. Concerning the PEG-free sample ($CaCl_2$ / SiO_2) after sorption, its forms larger and slightly harder aggregates than samples 1 and 2. More importantly, stratification was observed when the material was retrieved from the reactor. The lower part likely contains more salt than the upper part because it turned into a viscous gel within a couple of hours (Fig. 10), while the upper part was more stable. The rust-colored trails visible in Fig. 10 are likely due to iron oxides. Indeed, the PEG-free sample caused an important corrosion of the apparatus.

Fig. 9. Evolution of the appearance of sample 2: (left) initial appearance, (right) appearance after sorption #4

Fig. 10. Appearance of the PEG-free sample ($CaCl_2$ / SiO_2) after sorption #5: material retrieved from the (left) lower part and (right) upper part of the reactor

3.2 Water vapor sorption isotherms

The water vapor sorption isotherms of bulk $CaCl_2$ and of the composite samples (water uptake per gram of dehydrated sample) are shown in Fig. 11. As reported in [31], bulk $CaCl_2$ hydration proceeds via two step-like increases at $P_v/P_v^{sat} = 0.11$ and $P_v/P_v^{sat} = 0.22$ which indicate the formation of $CaCl_2{\cdot}2H_2O$ and $CaCl_2{\cdot}4H_2O$. The third step at $P_v/P_v^{sat} = 0.32$ is attributed to the formation of $CaCl_2{\cdot}6H_2O$ [32], followed by progressive salt deliquescence and water absorption by the salt solution [31]. As expected, the bulk salt presents higher water uptake and affinity for water vapor than the studied composite samples at $P_v/P_v^{sat} > 0.11$. However, pure $CaCl_2$ would melt if placed in the reactor under the chosen operating conditions ($P_v/P_v^{sat} = 0.42$).

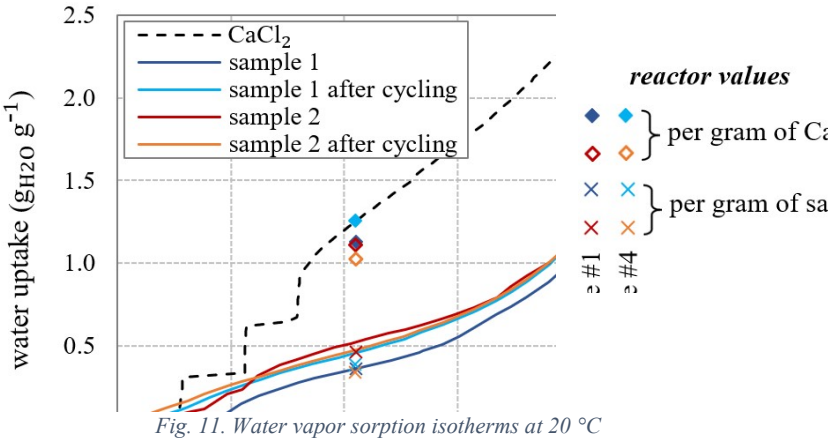

Fig. 11. Water vapor sorption isotherms at 20 °C

Before reactor cycling experiments, the sorption isotherms of samples 1 and 2 show a continuous increase of the water uptake with the relative water vapor pressure. An exponential growth is observed for $P_v/P_v^{sat} > 0.5$. The hydration steps of $CaCl_2$ incorporated in composite samples are hard to distinguish because the salt is not free but included in a $CaCl_2$ / PEG phase resulting from the complexation of the salt by the polymer. Two distinct steps may still be identified on the red curve (sample 2) at $P_v/P_v^{sat} = 0.15$ and 0.21. They possibly result from the formation of crystalline salt hydrates, as for bulk $CaCl_2$. As expected, fresh sample 2 exhibits a higher water uptake than fresh sample 1 over the entire vapor pressure range, corroborating the beneficial effect of a salt content increase on water sorption capacities in closed environments [33].

Despite unchanged salt content, the water uptake of sample 1 after cycling is greater than that of the fresh sample over the whole pressure range. This increased hydration ability of the incorporated salt may be explained by a reorganization of the salt after its dissolution inside the reactor, allowing easier access for water vapor molecules. For sample 2 after cycling, the water uptake change is minor compared to the fresh sample. The water uptake is slightly increased for $P_v/P_v^{sat} < 0.24$ and slightly decreased between 0.24 and 0.6. The higher hydration ability after cycling due to salt reorganization might counterbalance the water uptake reduction in sample 2 due to lower salt content after cycling experiments.

The water sorption capacity measured from reactor experiments and expressed by mass of dehydrated sample (cross-shaped markers) and by mass of $CaCl_2$ (diamond-shaped markers) are also indicated in Fig. 11. Cycles #1 and #4 only were represented, with the same colours as those used for the "fresh" and "after cycling" samples, respectively. The cross-shaped markers are close to the isotherm curves, especially for sample 1. The reactor values are thus consistent with those obtained from the 3Flex analyser, despite a 10 °C higher temperature during the sorption phase inside the reactor. The water uptake relative to the $CaCl_2$ content (diamond-shaped markers) is always above 1.0 g g^{-1}. This suggests the sorption of more than 6 mol of water per mol of calcium chloride inside the reactor and the deliquescence of part of the salt. In addition, nearly all the incorporated salt has certainly reacted with water because the markers are close to the bulk $CaCl_2$ isotherm.

3.3 TG-DSC results

3.3.1 Analysis of the weight loss and heat flow

The evolution of the mass measured by TGA during the second dehydration (section 2.3) is shown in Fig. 12 for samples 1 and 2 before and after reactor cycling experiments. The mass reduction during the temperature rise is caused by water loss and depends on the amount of water previously sorbed.

Before cycling experiments, sample 2 exhibits greater water loss than sample 1, which can be explained by its higher salt content, as observed in [34]. In addition, dehydration is slower for fresh

sample 2 than for fresh sample 1: the amount of water remaining in sample 2 after 30 min at 130 °C is 9% versus 4% for sample 1 due to smaller amount of salt in the latter. The water vapor diffusion resistance through sample 2 may also be increased because of its higher salt content.

After cycling experiments, the weight loss measured for sample 1 is reduced (compared to before cycling), but the difference is small. For sample 2, on the contrary, the dehydration curve after cycling is far from that of the fresh sample and the weight loss reduction is significant. This indicates a decrease in the amount of water sorbed during hydration, which is due to the loss of salt in sample 2 as a consequence of salt deliquescence and leakage during reactor experiments. The TGA results are thus consistent with the salt content evolution determined with ICP-OES (Table 2).

The corresponding heat flow signals (in W g^{-1} of dehydrated sample) obtained by DSC are presented in Fig. 13. Despite the presence of large amounts of salt, the composite materials exhibit a single endothermic signal during dehydration thanks to a homogeneous salt distribution in the samples (although overlapped signals cannot be completely excluded). The highest endothermic peak is observed for sample 2 before cycling. Its maximum is slightly shifted to high temperatures (116 °C vs 110 °C) compared to sample 1. This is due to the greater salt content of sample 2, generating both stronger interaction between the sample and water and an increased water vapor diffusion resistance. After cycling, sample 1 exhibits a more intense endothermic signal than the fresh sample. This can be explained by the salt reorganization already mentioned above, which increases accessibility to the salt and reduces water vapor diffusion resistance. For sample 2 after cycling, the endothermic peak intensity is reduced compared to the fresh sample due to the decreased amount of sorbed water inferred from Fig. 12 (which results from a salt content reduction). Lastly, quasi-simultaneous return of the heat flow to the baseline for sample 1 before and after cycling and for sample 2 after cycling can be attributed to similar salt contents for the three materials.

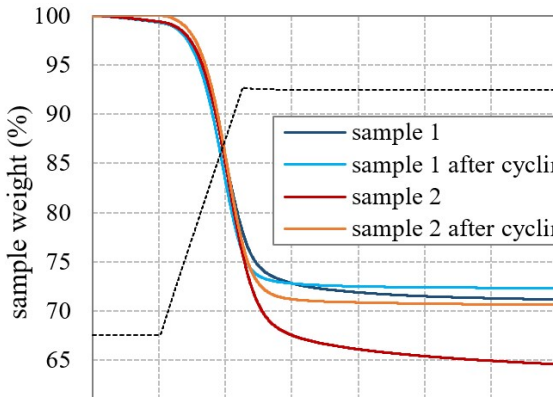

Fig. 12. Comparison of the weight loss during the second TGA dehydration for samples 1 and 2

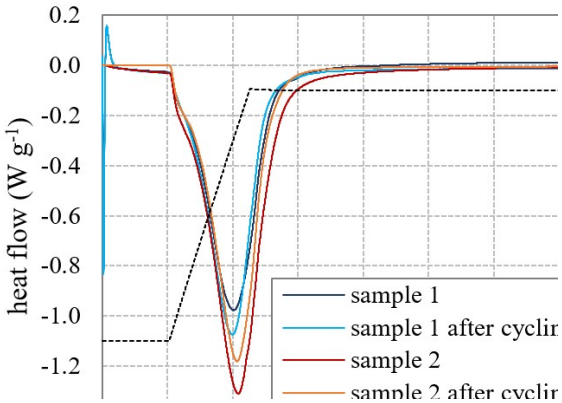

Fig. 13. DSC dehydration peaks during the second TGA dehydration for samples 1 and 2

3.3.2 Heat and water storage properties

The enthalpy of desorption and the water storage capacity of the tested samples (expressed by mass of dehydrated material) are presented in Table 3. Before cycling, sample 2 exhibits higher water sorption capacity and enthalpy of desorption than sample 1 (+ 40% and + 58%, respectively). This increase of water and heat storage capacities with the amount of salt has already been reported [11,35-36]. The performance improvement is however greater than the salt content increase (+ 31%). This is likely due to a good dispersion of the salt in the silica / PEG matrix, as shown previously by EDX analysis (Fig. 6). After cycling, the modification of the water and heat storage capacities of sample 1 is minor because the salt content is virtually unchanged. For sample 2, on the contrary, a drastic reduction of the water and heat storage capacities can be observed after cycling compared to the fresh sample (- 28% and - 30%, respectively), which is due to the loss of incorporated $CaCl_2$.

Table 3. Water and heat storage capacities of studied samples measured by TG-DSC

	water sorption capacity (g_{H2O} g^{-1})	enthalpy of desorption (kJ kg^{-1})	enthalpy of desorption (kJ mol^{-1}_{H2O})
Sample 1	0.414 ± 0.020	1019 ± 20	44.3 ± 2.3
Sample 1 after cycling	0.389 ± 0.020	1040 ± 20	48.2 ± 2.6
Sample 2	0.580 ± 0.020	1608 ± 20	49.9 ± 1.8
Sample 2 after cycling	0.419 ± 0.020	1118 ± 20	48.1 ± 2.5

The enthalpy of desorption per mol of water is also reported in Table 3 in order to evaluate the bonding strength between water molecules and sorbent. The values all exceed the vaporization enthalpy of water (39.1 kJ mol^{-1} at 130 °C), but they are lower than the dehydration enthalpy of pure $CaCl_2$ (about 60 kJ mol^{-1}) [11]. This suggests that water molecules bond both with the salt and to each other. In other words, multilayer sorption occurs. The desorption enthalpy increases for sample 1 after cycling experiments, which indicates stronger interaction than for the fresh sample. This phenomenon could be attributed to easier hydration and accessibility of the salt, promoting high energy salt-water bonding instead of multilayer water-water bonding. For sample 2 after cycling, the enthalpy is reduced by 4% compared to the fresh sample despite a 20% decrease in the salt content. In this case, the improved accessibility of the salt after cycling might counterbalance the salt loss. Indeed, the desorption enthalpy measured for sample 2 after cycling is similar to that of sample 1 after cycling, showing comparable strength of water-sorbent interaction.

A graphical comparison of water and heat storage capacities determined from TG-DSC and from reactor experiments is provided in Fig. 14 for the fresh samples and after cycling (referring to cycles #1 and #4 inside the reactor). The enthalpy of sorption in the reactor case is obtained from Eq. (7), which includes the heat loss. The uncertainty in the reactor values is large (around 20%). Besides, the mass of the sample analyzed by TGA amounts to 8 mg. Material inhomogeneities could therefore have a strong impact on the results. Some discrepancies may also be explained by a 5 °C lower temperature during the sorption phase in the TGA system than in the reactor. Despite these differences, the order of magnitude of the sorption capacities and of the enthalpies are consistent between both methods, with a maximum deviation of 20% and 16%, respectively. The evolution of the water and heat storage capacities between the fresh and "after cycling" samples are also relatively similar. The differences observed for fresh sample 2 could be due to salt leakage in the reactor during the first cycle. The values are indeed averaged over the whole sorption phase, but the sample is not really "fresh" anymore when the sorption is completed.

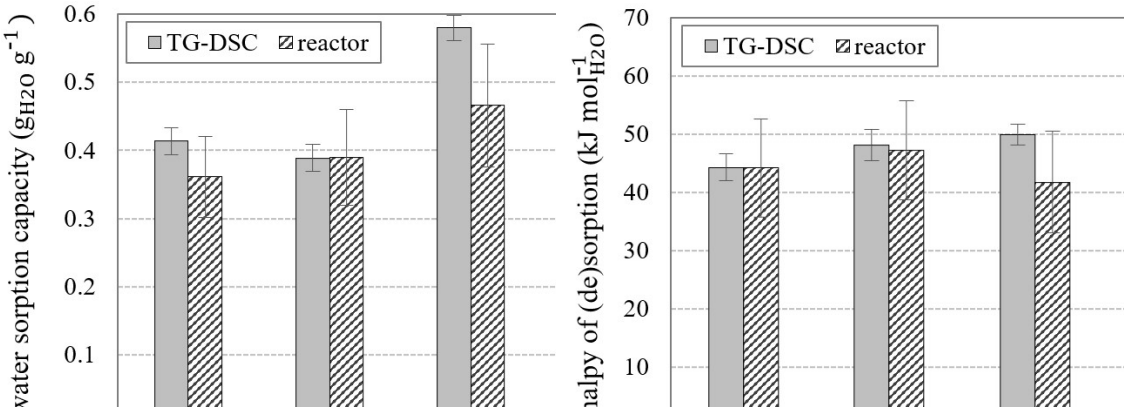

Fig. 14. Results comparison between TG-DSC and reactor experiments: (left) water sorption capacity and (right) enthalpy of (de)sorption

3.4 Lab-scale reactor cycling experiments

3.4.1 Sorption kinetics

The breakthrough curves are presented in Fig. 15 for the four cycles carried out in the reactor (described in section 2.2) with each sample. Such curves are used to characterize the sorption kinetics and to evaluate the sorption capacity of the tested materials. They are obtained from the ratio of the water outlet partial pressure $P_{v,out}$ to the water inlet partial pressure $P_{v,in}$.

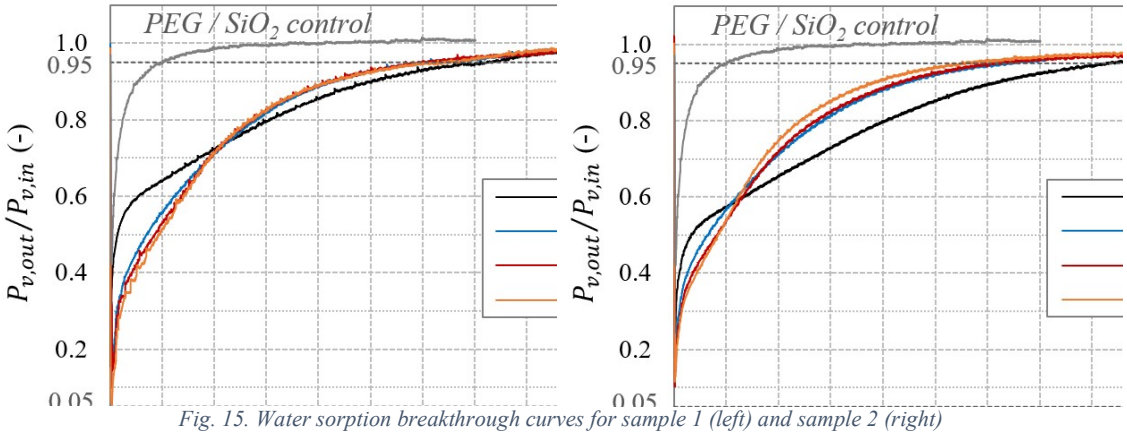

Fig. 15. Water sorption breakthrough curves for sample 1 (left) and sample 2 (right)

For both samples 1 and 2, the shape of the breakthrough curve is significantly altered between the first cycle (black solid line) and second cycle (blue line). This is probably due to a change in the initial properties of the material. The shift is greater for sample 2, likely because of deliquescence and salt leakage from the composite during the first cycle (as explained in section 3.4.2). After that, curves #2 to #4 are overlapping in both cases, showing that the cycles are nearly identical and that material properties are stable. Furthermore, comparison of the graphs shows that the sorption kinetics of samples 1 and 2 is comparable for cycles #2 to #4 despite different initial salt contents. This may be explained by salt leakage during the first cycle using sample 2, leading to a reduced salt content. The salt content of sample 2 after cycling approaches that of sample 1, as shown in section 3.1. Breakthrough takes place when the sorbate (water) starts to be detected at the outlet of the reactor. In this work, the breakthrough time was measured when the vapor outlet partial pressure reaches 5% of the vapor inlet pressure ($P_{v,out}/P_{v,in} = 0.05$). Breakthrough is immediate for both samples, which never fully sorb the water vapor provided at the inlet for the considered bed thickness. Regarding saturation ($P_{v,out}/P_{v,in} = 0.95$), it occurs after 12 h for cycles #2 to #4. For the first cycle, the sorption kinetics is slower when using sample 2 than sample 1 (saturation is reached after 16 h 30 versus 14 h 30), because of the higher initial salt content of the former, which also certainly increases the water vapor diffusion resistance in the beads.

Fig. 15 includes the breakthrough curve obtained with a similar mass of salt-free control sample for cycle #3 (grey line). The curve shows that the PEG / SiO_2 sample sorbs much less water than the others and is saturated after about two hours. The influence of the matrix will be further analyzed in the following sections.

The evolution of temperatures T_1 to T_5 over the sorption phase of cycle #4 is shown in Fig. 16 for the three tested samples. The temperature level is slightly decreased when using sample 2 instead of sample 1: the maximum temperature is around 49 °C in the former case and 54 °C in the latter. The difference is likely explained by the reduced final salt content of sample 2 compared to sample 1 because of deliquescence and salt leakage. The latter phenomenon has not occurred with sample 1. Concerning the salt-free control sample (PEG / SiO_2), the right graph shows that the temperatures rise up to 40 °C before a sharp decrease. They return to their initial value (~ 30 °C) after

two hours, when it takes more than eight hours for samples 1 and 2. The control test also highlights the heat loss from the reactor, as T_5 reaches 28.7 °C at the end of the test.

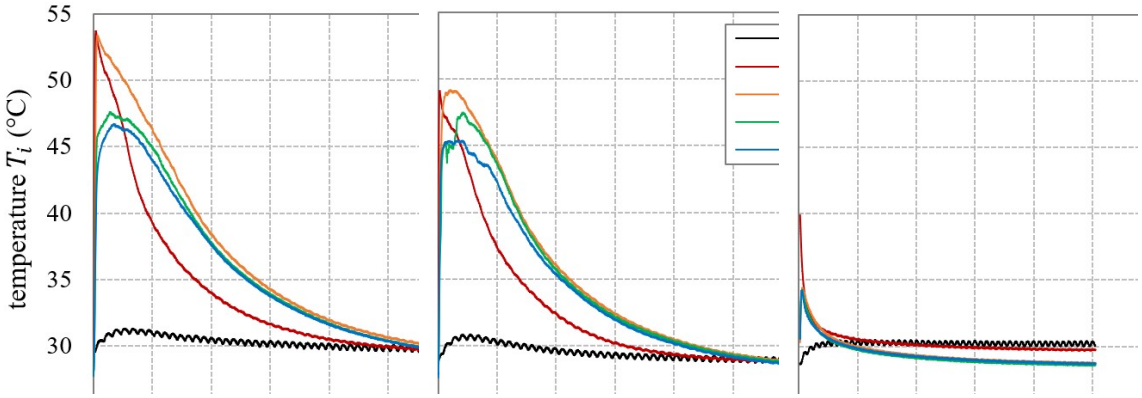

Fig. 16. Temperature curves over the sorption phase of cycle #4 for sample 1 (left), sample 2 (center) and the salt-free control (right)

3.4.2 Performance analysis at the reactor scale

The water sorption capacity of each sample is given in Table 4, as well as the generated energy and power during the sorption process for each cycle. Since the heat loss from the reactor is neglected in the calculation (eq. (3)), the generated energies and powers are systematically underestimated, but such a bias should not influence the following comparative analysis. The sorption capacity and the energy density are expressed by mass or by volume of dehydrated material (at 130 °C for four hours). The bulk density of the dry material is estimated to be 750 ± 150 kg m^{-3} for sample 1, 710 ± 70 kg m^{-3} for sample 2 and 720 ± 40 kg m^{-3} for the salt-free control sample (PEG / SiO_2). The uncertainty in each value is indicated in Table 4 following a plus or minus sign. The uncertainties are quite important, but cycling experiments conducted with zeolite have shown a good repeatability of measurements. The following comparative analysis is thus reliable. Some data of Table 4 is also presented in Fig. 17; namely, the water sorption capacity and the mass energy density. Cycles #2 and #4 are not included for the PEG / SiO_2 sample because of a malfunction of the hygrometers during those cycles. Still, the temperature curves proved comparable from cycle #1 to cycle #4.

Table 4. Evolution of the water sorption capacity and of the generated energy and power over several cycles for each sample (by mass or volume of dehydrated material)

	Sample 1					**Sample 2**					**PEG / SiO_2**		
cycle	#1	#2	#3	#4	**mean**	#1	#2	#3	#4	**mean**	#1	#3	**mean**
quantity of sorbed water m_w (g)	20.3 ± 2.8	20.9 ± 2.9	21.3 ± 3.2	21.9 ± 3.1	**21.1**	26.2 ± 4.4	20.3 ± 2.8	20.6 ± 4.0	19.0 ± 3.2	**21.5**	0.9 ± 2.1	1.5 ± 2.1	**1.2**
water sorption capacity (g_{H2O} g^{-1})	0.36 ± 0.06	0.37 ± 0.06	0.38 ± 0.07	0.39 ± 0.07	**0.37**	0.47 ± 0.09	0.36 ± 0.06	0.37 ± 0.08	0.34 ± 0.07	**0.38**	0.02 ± 0.04	0.03 ± 0.04	**0.02**
generated energy Q_{air} (kJ)	37.4 ± 1.9	44.9 ± 2.3	48.1 ± 2.5	45.6 ± 2.3	**44.0**	46.6 ± 2.4	41.9 ± 2.2	44.8 ± 2.3	41.0 ± 2.1	**43.6**	0.9 ± 0.1	0.8 ± 0.1	**0.9**
energy density (kJ kg^{-1})	665 ± 59	798 ± 70	856 ± 76	811 ± 71	**782**	829 ± 73	745 ± 66	797 ± 70	730 ± 65	**775**	17 ± 2	14 ± 2	**15**
energy density (kWh m^{-3})	131 ± 18	157 ± 21	169 ± 23	160 ± 22	**154**	173 ± 38	155 ± 34	166 ± 37	152 ± 34	**162**	3 ± 1	3 ± 1	**3**
maximum power $\dot{Q}_{air,max}$ (W)	1.7 ± 0.3	2.9 ± 0.3	3.1 ± 0.3	3.1 ± 0.3	**2.7**	2.2 ± 0.3	2.7 ± 0.4	2.9 ± 0.4	3.2 ± 0.4	**2.8**	0.7 ± 0.2	0.7 ± 0.2	**0.7**
power density (kW m^{-3})	21.3 ± 4.6	36.1 ± 5.8	38.8 ± 6.1	38.6 ± 6.1	**33.7**	29.8 ± 7.5	36.3 ± 9.4	39.2 ± 9.9	42.4 ± 10.5	**37.0**	9.2 ± 2.7	9.2 ± 2.7	**9.2**

The quantity of water sorbed by sample 1 is marginally altered from cycle #1 to cycle #4. The generated energy and power, however, increase significantly (+ 20% and + 70%) between the first and second cycles. This might be due to easier accessibility of the salt after the first cycle, promoting high-energy salt-water bonding instead of multilayer water-water bonding (as explained in section 3.3). From cycle #2 to cycle #4, the generated energy and power are more stable, with a maximum variation of 7% between cycles. These results are consistent with the modification of the sorption kinetics observed in Fig. 15 between the first cycle and the next ones. According to Fig. 15, the quantity of water sorbed during the first four hours of cycle #1 is reduced compared to that sorbed at the beginning of the next cycles, which explains the variation of the maximum power shown in Table 4. For sample 1, there is no performance degradation indicative of salt leakage. The host matrix manages to stabilize the hydrated calcium chloride under the chosen experimental conditions.

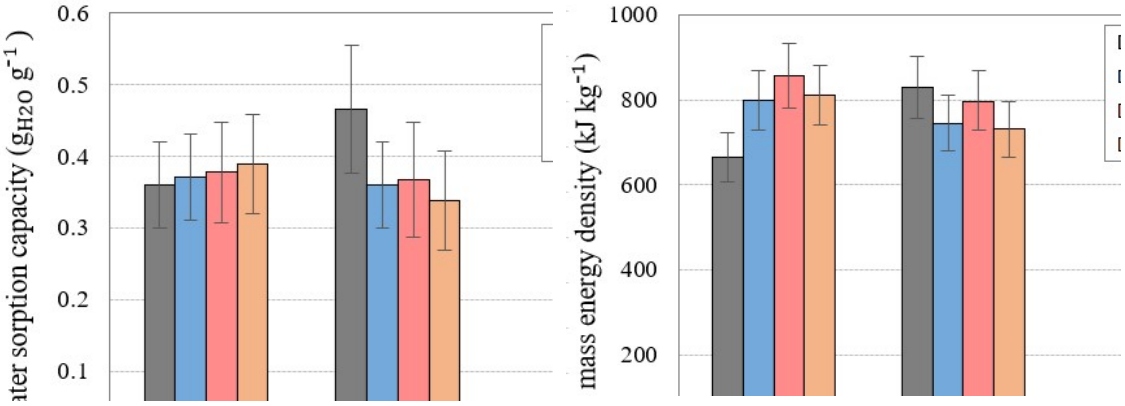

Fig. 17. Evolution of the water sorption capacity (left) and of the mass energy density (right) for each sample

For sample 2, the water sorption capacity decreases by 20% between the first and second cycles, while the generated energy is reduced by 10%. This performance degradation suggests that salt leakage occurred during the first cycle. From cycle #2 to cycle #4, the sorption capacity and energy density of sample 2 are approximately stable. Additional leakage is thus unlikely. Besides, the values are close to those measured with sample 1, probably because the final salt content of sample 2 is about that of sample 1 (section 3.1).

Results obtained using the salt-free control sample (PEG / SiO_2) show that the matrix contributes negligibly to the water sorption (6% on average) and to the energy generation (2%). The active sorption material is thus clearly calcium chloride or, more precisely, a $CaCl_2$ / PEG phase resulting from the coordination of the salt by the polymer (as suggested by the FTIR analysis in section 3.1). The water sorption capacity amounts on average to 0.37 g_{H2O} g^{-1} of dehydrated material for sample 1 and 0.38 g_{H2O} g^{-1} for sample 2, while the mass energy densities are 782 kJ kg^{-1} and 775 kJ kg^{-1}, respectively. Despite a higher initial salt content of sample 2, its heat storage performance is not improved compared to sample 1 because of salt leakage.

Additional experiments were conducted using a PEG-free control sample having the same $CaCl_2$ / SiO_2 proportion as sample 1 in order to assess the contribution of the polymer to salt stabilization. The water storage performance of the PEG-free sample ($CaCl_2$ / SiO_2) varied significantly over five cycles (Fig. 18), probably because of several modifications in the composite structure. Stratification was indeed observed when the material was retrieved from the reactor, as explained in section 3.1. The temperature measured during cycles #2 and #5 are also presented in Fig. 19 to illustrate the unpredictability of the results (the recording was interrupted during cycle #2 because of a power cut). Temperatures T_3 to T_5 are however not entirely reliable: they come from thermocouples placed above the sorbent bed on which a powder deposition composed mainly of salt was discovered. Indeed, some salt may have been entrained by the air flow during cycling and deposited on the sensors, thus influencing the results. Besides, the experiments with the PEG-free sample caused an important corrosion of the apparatus. This phenomenon did not occur when using

sample 1, showing that the PEG enhanced the stability of the material. At times, the PEG-free sample exhibited interesting storage performances but, ultimately, it proved unstable and inadequate for integration in a real application due to stratification and corrosion issues.

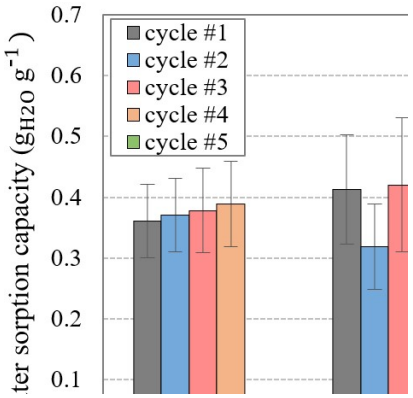

Fig. 18. Evolution of the water sorption capacity of $CaCl_2$ / SiO_2 compared to sample 1

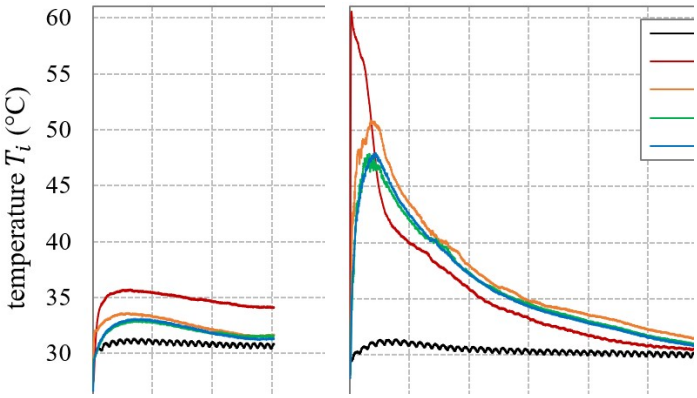

Fig. 19. Temperature curves over the sorption phase of cycle #2 (left) and cycle #5 (right) for the PEG-free control sample ($CaCl_2$ / SiO_2)

3.4.3 Comparison with zeolite 13X and other materials from the literature

A similar set of experiments was conducted using zeolite 13X BFK (Köstrolith® supplied by CWK, beads diameter from 1.2 to 2.0 mm,), which is a well-known material for heat storage applications [37-38]. Three cycles were realized in this case in order to compare the results with those obtained using the same mass of composite samples. The bulk density of zeolite is 800 ± 100 kg m^{-3}.

The sorption kinetics of the materials is compared in Fig. 20. In the zeolite case, all the curves overlapped, so only that of the last cycle is presented. The sorption kinetics of zeolite is much faster than that of samples 1 and 2: around 2 h 30 are required to reach saturation ($P_{v,out}/P_{v,in} = 0.95$) with zeolite, compared to 12 h for the composite samples. In the latter case, the sorption kinetics may be limited by chemical kinetics, heat transfer or by water mass diffusion across the sorbent. A slow sorption kinetics can be an advantage or a drawback depending on the considered application and the required power level. Incidentally, Fig. 20 also shows that breakthrough ($P_{v,out}/P_{v,in} = 0.05$) occurs after about 40 minutes when using zeolite, while it is immediate for samples 1 and 2. Zeolite is thus able to sorb almost all the provided water vapor during 40 minutes.

According to Fig. 21, the measured temperature during the sorption phase is up to 81 °C when using zeolite. The maximum temperature is thus 30 °C higher than with the composite samples. This difference can be partly explained by the faster sorption kinetics of zeolite. The temperatures return to their initial value after four hours with zeolite versus more than eight hours for samples 1 and 2 (Fig. 16).

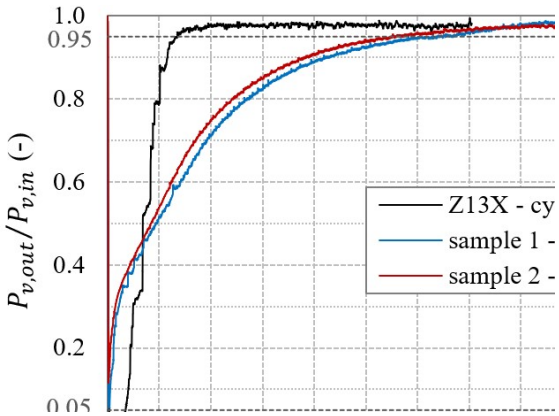

Fig. 20. Comparison of water sorption breakthrough curves of zeolite 13X and composite samples

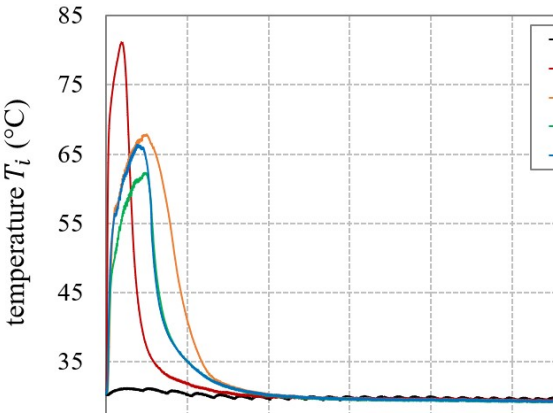

Fig. 21. Temperature curves over the sorption phase of cycle #3 for zeolite 13X

The performance comparison between zeolite and the composite samples is presented in Fig. 22 for the last conducted cycle in each case. The maximum generated power doubles when using zeolite instead of composite samples, which is consistent with the previous analysis of sorption kinetics and temperature curves. Still, the mass energy density of the composite samples is considerably higher than that of zeolite due to a greater sorption capacity and because of the desorption temperature. In particular, the sorption capacity of sample 1 is twice that of zeolite.

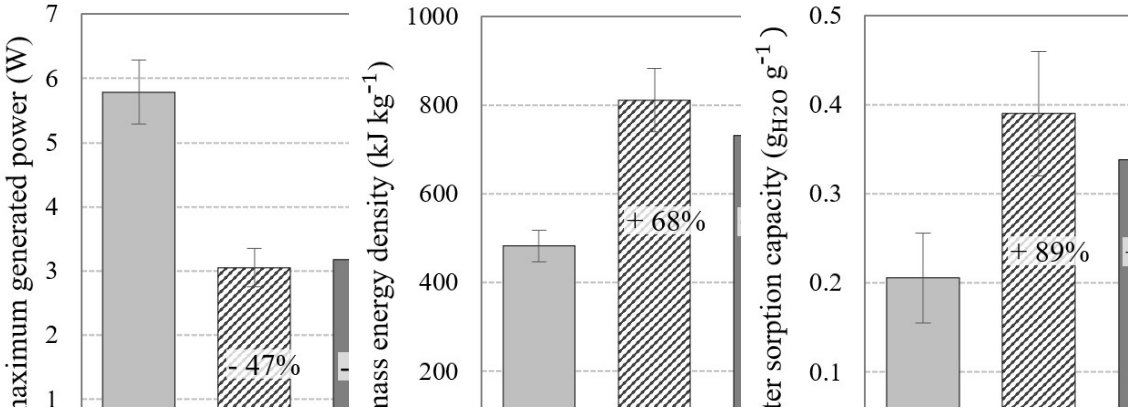

Fig. 22. Performance comparison of zeolite 13X (cycle #3) and composite samples (cycle #4): (left) maximum generated power, (center) mass energy density and (right) water sorption capacity

A comparison with other $CaCl_2$-based composite sorbents would be a valuable addition to the present analysis. Unfortunately, very few studies have been conducted in similar conditions. Skrylnyk *et al.* [12] synthetized a composite material containing 43 wt% of calcium chloride in a silica gel matrix. They charged 245 g of this dehydrated material into a lab-scale reactor and performed a sorption at 30 °C and 39% RH. The resulting energy density was 1110 kJ kg^{-1} (or 226 kWh m^{-3}). This value is somewhat higher than the mean energy density of samples 1 and 2 (Table 4), which can be explained by several differences in the experiments:

(1) The material was synthetized by Skrylnyk *et al.* [12,39] by impregnation of silica gel using an aqueous solution of $CaCl_2$, while samples 1 and 2 were synthetized by sol-gel method. The synthesis protocol influences the composite structure and the availability of the reactive salt.
(2) The air flow rate is 215 L min^{-1} in the study of Skrylnyk *et al.* [12], which is 6 times higher than in the present work relative to the sample mass. The flow rate affects the sorption kinetics and, as a result, the generated power and the temperature lift. Since the temperature determines the sorption equilibrium and enthalpy, the flow rate indirectly influences the energy density.
(3) About 70% of the sorbent layer surface is fluidized in the study of Skrylnyk *et al.* [12], which promotes the interaction with the air flow. The authors determined the energy density to be 145 kWh m^{-3} relative to the fluidized bed volume.
(4) The heat loss was neglected in both studies, but its impact in the present work may be greater because of a smaller reactor volume.

Concerning the sorption capacity, Skrylnyk *et al.* [12] provide a value of 0.4 g_{H2O} g^{-1}, which is similar to that measured here for samples 1 and 2 despite lower salt contents. Another research team [40-41] obtained an energy density of 1000 kJ kg^{-1} using 40 kg of composites made of silica gel and about 30-35 wt% $CaCl_2$. The authors mention that salt leakage possibly decreased the energy density of the sample with the highest salt content. Lastly, energy densities ranging from 1060 to 5140 kJ kg^{-1} (or 65 to 290 kWh m^{-3}) were measured with vermiculite as a matrix [42-44], but the salt content is not precisely stated in the corresponding studies. Table 5 summarizes the performance comparison of the cited $CaCl_2$-based composite materials.

Table 5. Comparison of $CaCl_2$-based composites tested in open thermochemical heat storage reactors

matrix material	$CaCl_2$ content (wt%)	dry sample mass (g)	water uptake ($g\ g^{-1}$)	average energy density ($kJ\ kg^{-1}$)	average energy density ($kWh\ m^{-3}$)	sorption temperature (°C)	RH (%)	desorption temperature (°C)	repeating cycles	Ref.
silica-PEG	32	56	0.37	782	154	30	42	130	4	this work
silica-PEG	42	56	0.38	775	162	30	42	130	4	this work
silica gel	43	245	0.4	1 110	226	30	39	150	1	[12]
silica gel	35	40 000	~ 0.7	1 000	224	15	-	90	500	[40]
silica gel	≲ 30	40 000	-	1 020	228	15	-	90	500	[41]
vermiculite	-	531	0.31	1 220	134	~ 16	~ 95	~ 90	4	[42]
vermiculite	≲ 43	~ 6 000	-	~ 5 140	290	21	75	-	1	[43]
vermiculite	-	125	-	1 060	65	19	78	-	1	[44]

4. Conclusion

This study aims at developing a stable and high energy density composite material for TCES. To this end, two composite sorbents based on silica, PEG and containing different amounts of calcium chloride were synthetized using the sol-gel method. The storage performance of each sample was characterized in a lab-scale open reactor in conditions of a solar heat storage system coupled with space heating. Salt-free (PEG / SiO_2) and PEG-free ($CaCl_2$ / SiO_2) controls were also tested. The main findings can be summarized as follows:

- The silica-PEG-$CaCl_2$ materials do not contain any micropores or mesopores (< 50 nm) and the distribution of constituents in the samples is homogeneous. Besides, the structural characterization showed the presence of a crystallized phase $CaCl_2$ / PEG resulting from the complexation of the salt by the polymer.
- With a regeneration temperature of 130 °C, sample 1 (32 wt% $CaCl_2$) exhibited an average water sorption capacity of 0.37 $g_{H2O}\ g^{-1}$ of dehydrated material and an energy density of 782 $kJ\ kg^{-1}$ (or 154 $kWh\ m^{-3}$) over four successive sorption cycles at 30 °C and 42% RH.
- Experiments on the salt-free control sample show that the PEG / SiO_2 matrix contributes negligibly to the water sorption and energy generation.
- The PEG / SiO_2 matrix managed to stabilize hydrated calcium chloride when the salt content was equal to 32 wt% despite the uptake of more than 6 mol of water per mol of salt and the deliquescence of part of the salt indicated by sorption isotherms.
- The storage performance of sample 2 (42 wt% $CaCl_2$) was not improved compared to sample 1 despite a higher initial salt content. This is due to salt leakage during the first cycle: the salt content decreased from 42 wt% to 33 wt%, according to elemental analysis.
- The sorption capacity of sample 1 is constant from cycles #1 to #4, but the generated energy increases significantly after the first cycle. Indeed, isotherm curves and TG-DSC measurement analysis suggest greater dispersion and accessibility of the salt after its dissolution in the reactor, promoting salt-water bonding rather than multilayer water-water bonding. As a result, the strength of water-sorbent interaction increases, as well as the energy generated by the sorption of a given amount of water. The enthalpy of desorption measured by TG-DSC after cycling is of about 48 $kJ\ mol_{H2O}^{-1}$, which is consistent with the value calculated from reactor experiments when considering the heat loss.
- When compared to zeolite 13X, the sorption kinetics of samples 1 and 2 is much slower. As a result, the maximum discharge temperature decreased from 80 °C to about 50 °C when using the composites instead of zeolite, and the generated power was halved. Still, the mass energy density of the composite sorbents is considerably higher than that of zeolite (+ 70% for sample 1 thanks to

a doubled sorption capacity), which makes them promising materials for heat storage applications with moderate required power outputs.

- The PEG-free control sample ($CaCl_2$ / SiO_2) exhibited interesting storage performances at times, but it proved unstable and inadequate for integration in a real application due to stratification and corrosion issues. These phenomena did not occur with the PEG-containing composite having the same $CaCl_2$ / SiO_2 proportion (sample 1), showing that the polymer enhanced the stability of the material.

A thorough characterization of the composites is needed to ensure stability under a wide range of operating conditions. Indeed, a change in temperature or humidity could promote salt deliquescence and leakage. Several tens of cycles should be performed to develop a meaningful trend for the material cyclic performance and stability. Another interesting prospect for future work is the testing of additional samples with different salt contents. This would enable the precise determination of the optimal composition and to achieve a deeper understanding of the composite performance and sorption kinetics. Ultimately, the composition of a sorbent material must be optimized according to numerous parameters including the storage performance, the cycling stability, the desired kinetics, as well as the cost of the material, its porosity and handling complexity. Important work remains to be done in achieving this multicriteria optimization.

Acknowledgments

This work was supported by the French National Research Agency (ANR) in the frame of the STOCK-CAR project (ANR-18-CE05-0044). The authors gratefully acknowledge the Ctμ platform of electron microscopy (Centre Technologique des Microstructures, Claude Bernard Lyon 1 University).

References

[1] IPCC. Climate change 2022: impacts, adaptation and vulnerability. Contribution of working group II to the sixth assessment report of the Intergovernmental Panel on Climate Change [Pörtner HO, Roberts DC, Tignor M, Poloczanska ES, Mintenbeck K, Alegría A, Craig M, Langsdorf S, Löschke S, Möller V, Okem A, Rama B (eds.)]. *Cambridge University Press*, Cambridge, UK and New York, USA, 2022, p. 3056. doi:10.1017/9781009325844.

[2] Connolly D, Lund H, Mathiesen BV, Werner S, Möller B, Persson U, Boermans T, Trier D, Østergaard PA, Nielsen S. Heat Roadmap Europe: combining district heating with heat savings to decarbonise the EU energy system. *Energy Policy* **65** (2014) 475-489. https://doi.org/10.1016/j.enpol.2013.10.035.

[3] European Commission. Communication from the Commission to the European Parliament, the Council, the European Economic and Social Committee and the Committee of the Regions - an EU Strategy on Heating and Cooling. Brussels, COM/2016/051 final (2016).

[4] Desai F, Prasad JS, Muthukumar P, Rahman MM. Thermochemical energy storage system for cooling and process heating applications: A review. *Energy Conversion and Management* **229** (2021) 113617. https://doi.org/10.1016/j.enconman.2020.113617.

[5] Lin J, Zhao Q, Huang H, Mao H, Liu Y, Xiao Y. Applications of low-temperature thermochemical energy storage systems for salt hydrates based on material classification: A review. *Solar Energy* **214** (2021) 149-178. https://doi.org/10.1016/j.solener.2020.11.055.

[6] Clark R-J, Mehrabadi A, Farid M. State of the art on salt hydrate thermochemical energy storage systems for use in building applications. *Journal of Energy Storage* **27** (2020) 101145. https://doi.org/10.1016/j.est.2019.101145.

[7] Zhao Q, Lin J, Huang H, Wu Q, Shen Y, Xiao Y. Optimization of thermochemical energy storage systems based on hydrated salts: A review. *Energy and Buildings* **244** (2021) 111035. https://doi.org/10.1016/j.enbuild.2021.111035.

[8] Hua W, Yan H, Zhang X, Xu X, Zhang L, Shi Y. Review of salt hydrates-based thermochemical adsorption thermal storage technologies. *Journal of Energy Storage* **56** (2022) 106158. https://doi.org/10.1016/j.est.2022.106158.

[9] Leng G, Navarro H, Yu Q, Wellio G, Qiao G, Li C, Huang Y, Zhao Y, Zhang G, Meng Y, Chang C, Li Y, Ding Y, Jiang Z, Cong L, Wang Y, Wei B, Wang Y, Wei B. Design of composite materials/devices for thermal storage – A critical review. *Veruscript Functional Nanomaterials* **2** (2018) 1-28. https://doi.org/10.22261/GHV5W9.

[10] Mohapatra D, Nandanavanam J. Salt in matrix for thermochemical energy storage - A review. *Materials Today: Proceedings* **72** (2023) 27-33. https://doi.org/10.1016/j.matpr.2022.05.453.

[11] Jabbari-Hichri A, Bennici S, Auroux A. Enhancing the heat storage density of silica-alumina by addition of hydgroscopic salts ($CaCl_2$, $Ba(OH)_2$ and $LiNO_3$), *Solar Energy Materials and Solar Cells* **140** (2015) 351-360. http://doi.org/10.1016/j.solmat.2015.04.032.

[12] Skrylnyk O, Courbon E, Heymans N, Frère M, Bougard J, Descy G. Performance characterization of salt-in-silica composite materials for seasonal energy storage design. *Journal of Energy Storage* **19** (2018) 320-336. https://doi.org/10.1016/j.est.2018.08.015.

[13] Silvester L, Touloumet Q, Kamaruddin A, Chassagneux F, Postole G, Auroux A, Bois L. Influence of silica functionalization on water sorption and thermochemical heat storage of mesoporous SBA 15/$CaCl_2$ composites. *ACS Applied Energy Materials* **4** (2021) 5944-5956. https://doi.org/10.1021/acsaem.1c00786.

[14] Barsk A, Yazdani MR, Kankkunen A, Seppälä A. Exceptionally high energy storage density for seasonal thermochemical energy storage by encapsulation of calcium chloride into hydrophobic nanosilica capsules. *Solar Energy Materials and Solar Cells* **251** (2023) 112154. https://doi.org/10.1016/j.solmat.2022.112154.

[15] Piperopoulos E, Calabrese L, Bruzzaniti P, Brancato V, Palomba V, Caprì A, Frazzica A, Cabeza LF, Proverbio E, Milone C. Morphological and structural evaluation of hydration/dehydration stages of $MgSO_4$ filled composite silicone foam for thermal energy storage applications. *Applied Sciences* **10** (2020) 453. https://doi.org/10.3390/app10020453.

[16] Van Ravensteijn BGP, Donkers PAJ, Ruliaman RC, Eversdijk J, Fischer HR, Huinink HP, Adan OCG. Encapsulation of salt hydrates by polymer coatings for low-temperature heat storage applications. *ACS Applied Polymer Materials* **3** (2021) 1712-1726. https://doi.org/10.1021/acsapm.0c01186.

[17] Aarts J, van Ravensteijn B, Fischer H, Adan O, Huinink H. Polymeric stabilization of salt hydrates for thermochemical energy storage. *Applied Energy* **341** (2023) 121068. https://doi.org/10.1016/j.apenergy.2023.121068.

[18] Zheng L, Zhang X, Hua W, Wu X, Mao F. The effect of hydroxylated multi-walled carbon nanotubes on the properties of Peg-$CaCl_2$ form-stable phase change materials. *Energies* **14** (2021) 1403. https://doi.org/10.3390/en14051403.

[19] Wu X, Shi S, Wang Y, Tang B, Guo L, Gao Y, Jiang T, Yang K, Sun K, Zhao Y, Li W, Yu J. Polyethylene glycol–calcium chloride phase change materials with high thermal conductivity and excellent shape stability by introducing three-dimensional carbon/carbon fiber felt. *ACS Omega* **6** (2021) 33033-33045. https://doi.org/10.1021/acsomega.1c05186.

[20] Li B, Shu D, Wang R, Zhai L, Chai Y, Lan Y, Cao H, Zou C. Polyethylene glycol/silica (PEG@SiO2) composite inspired by the synthesis of mesoporous materials as shape-stabilized phase change material for energy storage. *Renewable Energy* **145** (2020) 84-92. https://doi.org/10.1016/j.renene.2019.05.118.

[21] Nakanishi K, Tanaka N. Sol-gel with phase separation. Hierarchically porous materials optimized for high-performance liquid chromatography separations. *Accounts of Chemical Research* **40** (2007) 863-873. https://doi.org/10.1021/ar600034p.

[22] Wang W, Li T, Long H, Zhu L. Preparation of hierarchically mesoporous silica monolith using two components of poly(ethylene glycol) as cooperative dual-templates. *Journal of Non-Crystalline Solids* **461** (2017) 80-86. https://doi.org/10.1016/j.jnoncrysol.2017.02.001.

[23] Koreniuk A, Maresz K, Odrozek K, Jarzębski AB, Mrowiec-Białoń J. Highly effective continuous-flow monolithic silica microreactors for acid catalyzed processes. *Applied Catalysis A: General* **489** (2015) 203-208. https://doi.org/10.1016/j.apcata.2014.10.047.

[24] Guyot M, Daurat C, Vuillet-a-Ciles V, Pontille L, Le Porcher B, Chiriac R, Toche F, Chassagneux F, Toury B, Bois L. Foam silica films synthesized by calcium chloride-assisted emulsification. *Langmuir* **37** (2021) 4540-4549. https://doi.org/10.1021/acs.langmuir.1c00083.

[25] Bérut E, Outin J, Ondarts M, Lange H, Bois L, Le Pierrès N. Comparative experiments on a novel $CaCl_2$-based composite material and zeolite 13X inside a sorption reactor for solar heat storage. *ISES and IEA SHC International Conference on Solar Energy for Buildings and Industry (EuroSun2022)*, 25-29 September 2022, Kassel, Germany.

[26] Vengadesan E, Senthil R. A review on recent developments in thermal performance enhancement methods of flat plate solar air collector. *Renewable and Sustainable Energy Reviews* **134** (2020) 110315. https://doi.org/10.1016/j.rser.2020.110315.

[27] Joint Committee for Guides in Metrology. Evaluation of measurement data – Guide to the expression of uncertainty in measurement. JCGM 100:2008 (2008). http://www.bipm.org/utils/common/documents/jcgm/ JCGM_100_2008_E.pdf

[28] Bell IH, Wronski J, Quoilin S, Lemort V. Pure and pseudo-pure fluid thermophysical property evaluation and the open-source thermophysical property library CoolProp. *Industrial & Engineering Chemistry Research* **53** (2014) 2498-2508. https://doi.org/10.1021/ie4033999.

[29] Radhakrishnan S, Saini DR. Polymer-induced crystallization of inorganic salts II. PEO-$CaCl_2$, PEO-K_2CO_3 and PEO-$CaCO_3$. *Journal of crystal growth* **129** (1993) 191-201. https://doi.org/10.1016/0022-0248(93)90448-6.

[30] He L, Li J, Zhou C, Zhu H, Cao X, Tang B. Phase change characteristics of shape-stabilized PEG/SiO_2 composites using calcium chloride-assisted and temperature-assisted sol gel methods. *Solar Energy* **103** (2014) 448-455. https://doi.org/10.1016/j.solener.2014.02.042.

[31] Touloumet Q, Silvester L, Bois L, Postole G, Auroux A. Water sorption and heat storage in $CaCl_2$ impregnated aluminium fumarate MOFs. *Solar Energy Materials and Solar Cells* **231** (2021) 111332. https://doi.org/10.1016/j.solmat.2021.111332.

[32] Patek J, Klomfar J, Souckova M. Solid-liquid equilibrium in the system of $CaCl_2$-H_2O with special regard to the transition points. *Journal of Chemical and Engineering* Data **53** (2008) 2260-2271. https://doi.org/10.1021/je800009w.

[33] Nonnen T, Beckert S, Gleichmann K, Brandt A, Unger B, Kerskes H, Mette B, Bonk S, Badenhop T, Salg F, Glaser R. A thermochemical long-term storage system based on a salt/zeolite composite, *Chemical Engineering and Technology* **39** (2016) 2427-2434. https://doi.org/10.1002/ceat.201600301.

[34] Touloumet Q, Postole G, Silvester L, Bois L, Auroux A. Hierarchical aluminium fumarate metal-organic framework – alumina host matrix: Design and application to CaCl2 composites for thermochemical heat storage. *Journal of Energy storage* **50** (2022) 104702. https://doi.org/10.1016/j.est.2022.104702.

[35] Permyakova A, Wang S, Courbon E, Nouar F, Heymans N, D'Ans P, Barrier N, Billemont P, De Weireld G, Nathalie S, Frère M, Serre C. Design of salt-metal organic framework composites for seasonal heat storage applications. *Journal of Material Chemistry A* **5** (2017) 12889. https://doi.org/10.1039/c7ta03069j.

[36] Ristic A, Zabukovec Logar N. New composite water sorbents $CaCl_2$-PHTS for low-temperature sorption heat storage: determination of structural properties. *Nanomaterials* **9** (2019) 27. http://doi.org/10.3390/nano9010027.

[37] Helaly HO, Awad MM, El-Sharkawy II, Hamed AM. Theoretical and experimental investigation of the performance of adsorption heat storage system. *Applied Thermal Engineering* **147** (2019) 10-28. https://doi.org/10.1016/j.applthermaleng.2018.10.059.

[38] Kuznik F, Johannes K, Obrecht C, David D. A review on recent developments in physisorption thermal energy storage for building applications. *Renewable and Sustainable Energy Reviews* **94** (2018) 576-86. https://doi.org/10.1016/j.rser.2018.06.038.

[39] Courbon E, D'Ans P, Permyakova A, Skrylnyk O, Steunou N, Degrez M, Frère M. Further improvement of the synthesis of silica gel and $CaCl_2$ composites: Enhancement of energy storage density and stability over cycles for solar heat storage coupled with space heating applications. *Solar Energy* **157** (2017) 532-541. https://doi.org/10.1016/j.solener.2017.08.034.

[40] Zhu D, Wu H, Wang S. Experimental study on composite silica gel supported $CaCl_2$ sorbent for low grade heat storage. *International Journal of Thermal Sciences* **45** (2006) 804-813. https://doi.org/10.1016/j.ijthermalsci.2005.10.009.

[41] Wu H, Wang S, Zhu, D. Effects of impregnating variables on dynamic sorption characteristics and storage properties of composite sorbent for solar heat storage. *Solar Energy* **81** (2007) 864-871. https://doi.org/10.1016/j.solener.2006.11.013.

[42] Casey SP, Aydin D, Riffat S, Elvins J. Salt impregnated desiccant matrices for 'open' thermochemical energy storage – Hygrothermal cyclic behaviour and energetic analysis by physical

experimentation. *Energy and Buildings* **92** (2015) 128-139. https://doi.org/10.1016/j.enbuild.2015.01.048.

[43] Aydin D, Casey SP, Chen X, Riffat S. Novel "open-sorption pipe" reactor for solar thermal energy storage. *Energy Conversion and Management* **121** (2016) 321-334. https://doi.org/10.1016/j.enconman.2016.05.045.

[44] Sutton RJ, Jewell E, Elvins J, Searle JR, Jones P. Characterising the discharge cycle of $CaCl_2$ and $LiNO_3$ hydrated salts within a vermiculite composite scaffold for thermochemical storage. *Energy and Buildings* **162** (2018) 109-120. https://doi.org/10.1016/j.enbuild.2017.11.068.

Nomenclature

c_p	specific heat capacity at constant pressure, J K^{-1} kg^{-1} of dry air
k	leak coefficient, eq. (6)
m	mass, kg
$\dot{m}$	mass flow rate, kg s^{-1}
$\bar{M}$	molar weight, kg mol^{-1}
P	pressure, Pa
P_v	water vapor partial pressure, Pa
Q_{air}	sensible heat given to the air flow, J
$\dot{Q}_{air}$	heat transfer rate, W
Q_{loss}	heat loss, J
t	time, s
T	temperature, °C
T_i	i^{th} temperature measurement along the reactor, °C
$\bar{T}$	average of temperatures T_1 to T_4, °C
U	overall heat transfer coefficient between the ambient and the reactor, W K^{-1}
$\dot{V}$	volumetric flow rate, m^3 s^{-1}
W	sample weight, kg
x	specific humidity, kg of water vapor per kg of dry air

Greek symbols

ΔH_s	enthalpy of sorption, J mol^{-1} of water
λ	wavelength, m
ρ	density, kg m^{-3}

Subscripts and superscripts

amb	ambient conditions
da	dry air
ds	dry sample
ha	humid air
hs	hydrated sample
$hygro$	hygrometer
in	reactor inlet
$leak$	air leakage
max	maximum
out	reactor outlet

sat	saturated humid air
tot	total
w	sorbed water

Acronyms

AES	alkaline earth silicate
DSC	differential scanning calorimeter
EDS	energy dispersive spectrometry
FTIR	Fourier-transform infrared spectroscopy
ICP-OES	inductively coupled plasma optical emission spectroscopy
PCM	phase change material
PEG	polyethylene glycol
RH	relative humidity
SEM	scanning electron microscopy
TEOS	tetraethyl orthosilicate
TG(A)	thermogravimetric (analysis)
XRD	X-ray diffraction